SCIENCE CHINA
Chemistry

•ARTICLES•

https://doi.org/10.1007/s11426-024-2275-2

Enhancing solid-state lithium metal battery performance *via* indium-based modification of electrolytes and lithium metal surfaces: mechanistic insights and optimization

Zhongkai Wu[1,2], Chen Liu[1], Ziling Jiang[1,2], Lin Li[1,2], Siwu Li[3], Chaochao Wei[1,2], Qiyue Luo[1,2], Xia Chen[1], Long Zhang[4], Shijie Cheng[1] & Chuang Yu[1*]

[1]*State Key Laboratory of Advanced Electromagnetic Engineering and Technology, School of Electrical and Electronic Engineering, Huazhong University of Science and Technology, Wuhan 430074, China;*
[2]*School of Chemistry and Chemical Engineering, Huazhong University of Science and Technology, Wuhan 430074, China;*
[3]*Interdisciplinary Research Center of Smart Sensors, Academy of Advanced Interdisciplinary Research, Xidian University, Xi'an 710126, China;*
[4]*College of Physics and Energy, Fujian Normal University, Fuzhou 350117, China*

Received May 15, 2024; accepted August 27, 2024; published online September 4, 2024

Argyrodite-based solid-state lithium metal batteries exhibit significant potential as next-generation energy storage devices. However, their practical applications are constrained by the intrinsic poor stability of argyrodite towards Li metal and exposure to air/moisture. Therefore, an indium-involved modification strategy is employed to address these issues. The optimized doping yields a high Li-ion conductivity of 7.5 mS cm^{-1} for $Li_{5.54}In_{0.02}PS_{4.47}O_{0.03}Cl_{1.5}$ electrolyte, accompanied by enhanced endurance against air/moisture and bare Li metal. It retains 92.0% of its original conductivity after exposure to air at a low dew point of −60 °C in dry room. Additionally, a composite layer comprising Li–In alloy and LiF phases is generated on the surface of lithium metal anode via the reaction between InF_3 and molten Li. This layer effectively mitigates Li dendrite growth by creating a physical barrier from the robust LiF phase, while the Li–In alloy induces uniform Li-ion deposition and accelerates Li transport dynamics across the interphase between the solid electrolyte/Li metal. Moreover, the In-doped electrolyte facilitates the *in-situ* generation of Li–In alloy within its voids, reducing local current density and further inhibiting lithium dendrite growth. Consequently, the combination of the $Li_{5.54}In_{0.02}PS_{4.47}O_{0.03}Cl_{1.5}$ electrolyte and the InF_3@Li anode provides exceptional electrochemical performances in both symmetric cells and solid-state lithium metal batteries across different operating temperatures. Specifically, the $LiNbO_3$@$LiNi_{0.7}Co_{0.2}Mn_{0.1}O_2$/$Li_{5.54}In_{0.02}PS_{4.47}O_{0.03}Cl_{1.5}$/$InF_3$@Li cell delivers a high discharge capacity of 167.8 mAh g^{-1} at 0.5 C under 25 °C and retains 80.0% of its initial value after 400 cycles. This work offers a viable strategy for designing functional interfaces with enhanced stability for sulfide-based solid-state lithium batteries.

$Li_{5.5}PS_{4.5}Cl_{1.5}$ solid electrolyte, In_2O_3 dual-doping, InF_3 surface-modification, chemical/electrochemical stability, electrochemical performance

Citation: Wu Z, Liu C, Jiang Z, Li L, Li S, Wei C, Luo Q, Chen X, Zhang L, Cheng S, Yu C. Enhancing solid-state lithium metal battery performance *via* indium-based modification of electrolytes and lithium metal surfaces: mechanistic insights and optimization. *Sci China Chem*, 2024, 67, https://doi.org/10.1007/s11426-024-2275-2

*Corresponding author (email: cyu2020@hust.edu.cn)

© Science China Press 2024

1 Introduction

The rapid development of electric vehicles and large-scale energy storage systems urgently needs batteries that can deliver superior safety and elevated energy densities. However, the prevalent commercial lithium-ion batteries (LIBs) utilizing combustible organic electrolytes with limited electrochemical windows fail to fulfill the above demands [1,2]. Owing to the integration of inflammable inorganic solid-state electrolytes with wide electrochemical windows, as well as high-energy-density Li metal anodes [3], all-solid-state Li metal batteries (ASSLMBs) become an ideal candidate for future energy storage systems with high safety and high energy density [4–6]. Solid-state electrolytes (SSEs), as integral components of solid state batteries (SSBs), exert a profound influence on the overall performance of SSBs. To date, extensive endeavors have been dedicated to exploring SSEs with superior ionic conductivity and chemical/electrochemical stability. Among these SSEs, chlorine-based argyrodite sulfide SSEs are distinguished by high ionic conductivity, low grain boundary resistance, and easy processability, which hold promise for building ASSLMBs [7–14].

Li metal anodes, renowned for their high theoretical specific capacity (3,860 mAh g^{-1}) and low electrochemical potential (−3.04 V vs. standard hydrogen electrode), are considered as one of the most promising anodes for SSBs [15]. The integration of Li anodes with advanced cathode materials, such as ternary layered oxides, positions sulfide SSEs as a vital component for SSBs with high safety and high energy density [16,17]. However, the development of argyrodite-based SSEs is currently hindered by several key challenges, especially their air stability and compatibility with Li [18]. The air stability for sulfide electrolytes is a critical concern due to their hygroscopic nature, which can cause the generation for toxic hydrogen sulfide (H_2S) and material degradation [16]. Previous research revealed that the air stability of sulfide electrolytes can be enhanced via the multiple-element-doping strategy [19–21]. Fan's group [22] developed Bi–O co-doped argyrodite-based electrolyte. Evidently, with appropriate Bi and O co-substitution, not only high ionic conductivity but also good air stability could be achieved in the final $Li_{6.04}P_{0.98}Bi_{0.02}S_{4.97}O_{0.03}Cl$ electrolyte. Our previous work has further confirmed the merits of O doping in enhancing the air stability of SSEs [23]. Through an ambient air exposure, the variations in both phase composition and ionic conductivity of the electrolyte were investigated, yielding insights into the factors that contribute to the electrolyte's stability. Additionally, lowering the dew point is essential for improving the stability of sulfide electrolytes against air and moisture [18]. However, current related research lacks extensive and detailed experimental data.

The interfacial compatibility between argyrodite-based SSEs and Li metal anodes remains another critical issue. Theoretical [24] and experimental [25] results have proven the unstability of SSEs/Li interface, which causes a sluggish Li-ion migration dynamics and Li dendrite formation in grain boundaries or voids in SSEs [26]. These factors limit the electrochemical performance of ASSLMBs and introduce safety hazards. Lithium–indium (Li–In) alloy anodes have emerged as a common solution to enhance the compatibility [27]. The alloy's ability to form solid solutions and undergo minimal phase changes during lithiation/delithiation is beneficial for dendrite suppression [28]. However, high cost of In and elevated working potential of the alloy (0.6 V higher than that of Li) seriously decrease ASSLMBs' energy density and economic viability [29]. Therefore, reducing In content within sulfide-based ASSLMBs is of significant importance [30].

Improving the interfacial stability between sulfide SSEs and Li anodes is a critical challenge in the advancement of ASSLMBs. The goal can be achieved by either SSE modification or interfacial engineering on Li anodes [31]. Recent studies, including those by Jin *et al*. [32], have demonstrated that the *in-situ* growth of alloy phases, such as Li–Ag, at the Li/SSE interface, can greatly enhance Li transport and wettability, guaranteeing uniform and safe Li deposition [33,34]. Similarly, Li–In, Li–Zn/Li–Bi alloys at the interface and electrolyte grain boundaries have also been shown to enhance the compatibility of sulfide-based SSEs with Li [35,36]. To further stabilize the Li/SSE interface, dual doping sulfide electrolytes with In and O has been proposed. This modification introduces a small amount of In and O into the electrolyte, which, based on the hard-soft acid-base (HSAB) theory, can enhance electrolyte's stability [37]. However, the efficacy of single modifications is often limited, suggesting that a combination of electrolyte doping and anode surface treatment may be necessary to achieve the desired stability and performance [38]. Conclusively, the In-modification strategy, when applied to both argyrodite electrolyte and Li metal anode, may act synergistically to improve the electrochemical stability of a full cell. In this way, Li dendrite growth can be effectively suppressed both at interface and grain boundaries, thereby ensuring a good contact between Li and SSE.

At extreme ambient temperatures, the performance of power and energy storage batteries can be significantly influenced. Unfortunately, liquid electrolytes are more susceptible to temperature variations. At high temperatures, they are prone to safety hazards. At low temperatures, they suffer from a drastic reduction in ionic mobility [39]. In contrast, SSEs offer superior thermal stability and increased ionic conductivity at high temperatures [40]. Moreover, low temperatures only make a milder impact on SSEs. Besides, the Li plating/stripping behavior within SSBs under various temperatures remains ongoing investigation. The impact of temperature on the nucleation and growth of Li at low

temperatures, and the associated effects on battery performance, are not yet fully understood. Therefore, the development of ASSLMBs capable of operating efficiently across a broad temperature range is a complex but critical challenge.

Herein, we report a dual In-involved modification strategy designed specifically for Li metal batteries. First, a promising electrolyte of $Li_{5.54}In_{0.02}PS_{4.47}O_{0.03}Cl_{1.5}$ was successfully fabricated through the In–O co-doping method. Experiment and theoretical calculation demonstrate its greatly improved Li compatibility and air stability. Second, the method involves the acquisition of a Li–In–F composite by introducing InF_3 into the molten state of lithium. The *in-situ* generated Li–In alloys and LiF nanoparticles are homogeneously dispersed within the bulk Li, effectively regulating the Li plating and stripping behavior at the SSE/Li interface. Combined with In–O co-doping and InF_3 modification strategies, the splendid Li metal compatibility and the ability to suppress dendrite growth of In-involved modifications are demonstrated through long-term cycling performance of symmetric cells and full cells. Moreover, their potential applications in LMBs with wide operating temperature range are proved.

2 Results and discussion

Figure 1a demonstrates the X-ray diffraction (XRD) patterns for the prepared series of In–O dual doped choline-rich argyrodite $Li_{5.5+2x}In_xP_{1-x}S_{4.5-1.5x}O_{1.5x}Cl_{1.5}$ (x=0, 0.02, 0.05, 0.10) electrolytes, denoted as In-x (x=0, 0.02, 0.05, 0.10). When the dopant amount is low (x=0, 0.02, 0.05), the major diffraction peaks for these samples are well indexed to the pure cubic argyrodite structure (Li_7PS_6, PDF#0868), with no obvious impurity phases in the pattern. This suggests the successful fabrication for the target In–O co-doped electrolytes. However, upon the further increase in dopant concentration (x=0.1), clear peaks belonging to impurity phases are observed (Figure 1a). As depicted in Figure 1b, the introduction of In–O into the structure results in the substitution of P and S in the $Li_{5.5}PS_{4.5}Cl_{1.5}$ structure with In and O, respectively. XRD refinement was conducted on $Li_{5.5}PS_{4.5}Cl_{1.5}$ and $Li_{5.54}In_{0.02}P_{0.98}S_{4.47}O_{0.03}Cl_{1.5}$ to reveal the structure changes. During the XRD Rietveld refinement process, the above-mentioned substitution condition was fixed. Moreover, due to the poor stability of sulfide electrolytes towards air/moisture, during the XRD analysis, we shielded the sulfide surface with a plastic film, which inadvertently introduces a peak near 20 degrees, corresponding to the film's characteristic diffraction. So we have excluded the peak to prevent any interference from this peak on our XRD Rietveld refinement results. As shown in Figure 1c, d, the low R_{wp} and R_p values of these refinements suggests good fit for both electrolytes. The obtained lattice parameter value, a, for the pristine $Li_{5.5}PS_{4.5}Cl_{1.5}$ and $Li_{5.54}In_{0.02}P_{0.98}S_{4.47}O_{0.03}Cl_{1.5}$ is 9.8083 and

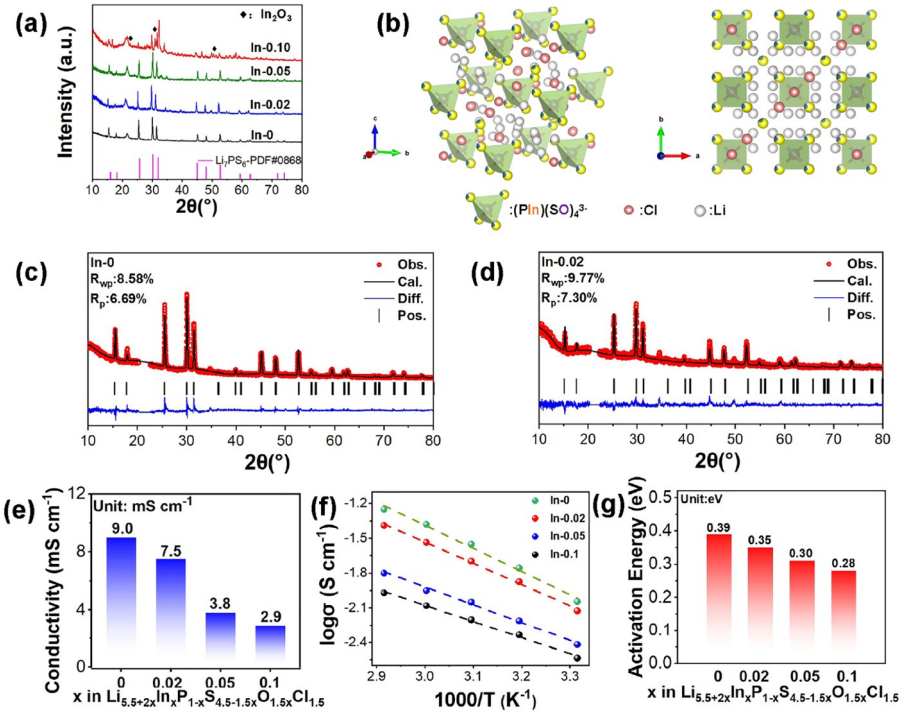

Figure 1 (Color online) (a) XRD patterns of the prepared $Li_{5.5+2x}In_xP_{1-x}S_{4.5-1.5x}O_{1.5x}Cl_{1.5}$ (x=0, 0.02, 0.05, and 0.10) materials. (b) Crystal structure of the In-doped $Li_{5.5}PS_{4.5}Cl_{1.5}$ electrolyte. XRD refinements of (c) $Li_{5.5}PS_{4.5}Cl_{1.5}$ and (d) $Li_{5.54}In_{0.02}PS_{4.47}O_{0.03}Cl_{1.5}$. (e) Room-temperature Li-ion conductivity changes of the synthesized materials as a function of the amount of In–O dopants. (f) Arrhenius plots and (g) corresponding activation energy variations deduced from the temperature-dependent conductivity of these $Li_{5.5+2x}In_xP_{1-x}S_{4.5-1.5x}O_{1.5x}Cl_{1.5}$ (x=0, 0.02, 0.05, and 0.1) electrolytes.

9.8073, respectively. It appears that In–O co-doping method leads to a decrease in the lattice parameters of $Li_{5.5}PS_{4.5}Cl_{1.5}$. Ionic conductivity of the prepared $Li_{5.5+2x}In_xP_{1-x}S_{4.5-1.5x}O_{1.5x}Cl_{1.5}$ (x=0, 0.02, 0.05, 0.10) was determined using the AC impedance method, employing stainless steel as the blocking electrodes. The Li-ion conductivity of $Li_{5.5+2x}In_xP_{1-x}S_{4.5-1.5x}O_{1.5x}Cl_{1.5}$ electrolytes is 9.0, 7.5, 3.8 and 2.9 mS cm^{-1} for x=0, 0.02, 0.05 and 0.10, respectively (Figure 1e). The temperature-dependent ionic conductivity results depicted in Figure 1f further confirm that an increase in the amount of In–O dual dopants leads to decreased Li-ion conductivities at various temperatures. Moreover, a rise of In–O dopant concentration results in reduced activation energy values for these electrolytes (Figure 1g). Given the trends in Figure 1e, g, it becomes apparent that the Li-ion conductivity for In–O co-doped $Li_{5.5}PS_{4.5}Cl_{1.5}$ SEs is influenced by factors beyond just activation energy. The compatibility of these custom-designed electrolytes with bare Li metal was further determined by the critical current density (CCD) values collected from the corresponding Li/solid electrolyte/Li symmetrical cells. As exhibited at Figure S1, the CCD values for the $Li_{5.5}PS_{4.5}Cl_{1.5}$, $Li_{5.54}In_{0.02}P_{0.98}S_{4.47}O_{0.03}Cl_{1.5}$, $Li_{5.60}In_{0.05}P_{0.95}S_{4.425}O_{0.075}Cl_{1.5}$, and $Li_{5.70}In_{0.10}P_{0.90}S_{4.35}O_{0.15}Cl_{1.5}$ electrolytes are 0.1, 1.8, 0.9 and 0.5 mA cm^{-2}, respectively. A higher CCD value of solid electrolytes indicates a potentially better Li metal compatibility. Therefore, the $Li_{5.54}In_{0.02}P_{0.98}S_{4.47}O_{0.03}Cl_{1.5}$ electrolyte was chosen for further investigation.

To assess the chemical stability for the In–O doped electrolyte with air/moisture, Li-ion conductivity, structural alterations, and release of side products were monitored for both $Li_{5.5}PS_{4.5}Cl_{1.5}$ and $Li_{5.54}In_{0.02}PS_{4.47}O_{0.03}Cl_{1.5}$ electrolytes under varying conditions. Firstly, H_2S generation amount of both electrolytes after the exposure to air (relative humidity or RH of 30%, room temperature) for 20 min was detected. Figure 2a shows that $Li_{5.5+2x}In_xP_{1-x}S_{4.5-1.5x}O_{1.5x}Cl_{1.5}$ electrolytes exhibit an obvious decline in the rate and amount of H_2S generation compared to bare $Li_{5.5}PS_{4.5}Cl_{1.5}$. This indicates that the In–O dual-doping method can enhance the air/moisture endurance for argyrodite solid electrolytes. With a slightly larger amount of In_2O_3, the obtained $Li_{5.54}In_{0.02}PS_{4.47}O_{0.03}Cl_{1.5}$ electrolyte shows a significant decrease in the H_2S generation rate and amount. When the dopant increases even more, such as $Li_{5.5+2x}In_xP_{1-x}S_{4.5-1.5x}O_{1.5x}Cl_{1.5}$ (x = 0.05 and 0.1), these materials exhibit comparable air/moisture stability as $Li_{5.54}In_{0.02}PS_{4.47}O_{0.03}Cl_{1.5}$ electrolyte. In terms of the amount of H_2S, the air stability is increased by nearly 2 times. This indicates that with a large In–O doping amount, the electrolyte shows a similar H_2S generation rate and quantity to that with a minor amount (x=0.02). Two possible explanations are introduced for this improvement of moisture stability. (1) The higher electronegativity of O than S and the stronger P–O bonding ability than P–S of the doped materials result in enhanced stability towards moisture; (2) the soft acid In are easier to bond with soft base S than P based on the classic soft and hard acid–base theory [23,41]. Thus the amount of In–O dopant has a slight effect on air/moisture stability for $Li_{5.5}PS_{4.5}Cl_{1.5}$. Subsequently, both $Li_{5.5}PS_{4.5}Cl_{1.5}$ and $Li_{5.54}In_{0.02}PS_{4.47}O_{0.03}Cl_{1.5}$ electrolyte pellets were subjected to an atmospheric exposure under a humidity level of 30% for 20 min. In this case (Figure 2b), notable bulges resulting from the side reaction between sulfide and ambient moisture are observed on the surface for the exposed $Li_{5.5}PS_{4.5}Cl_{1.5}$ pellet, whereas the $Li_{5.54}In_{0.02}PS_{4.47}O_{0.03}Cl_{1.5}$ pellet remains intact. Furthermore, for $Li_{5.5}PS_{4.5}Cl_{1.5}$ (Figure 2c), the major diffraction peaks attributed to cubic argyrodite phase disappear after 20-min air exposure. In contrast, the predominant XRD peaks indexed to the argyrodite phase remain evident in the pattern of the exposed $Li_{5.54}In_{0.02}PS_{4.47}O_{0.03}Cl_{1.5}$ electrolyte. These results validate the superior resilience of $Li_{5.54}In_{0.02}PS_{4.47}O_{0.03}Cl_{1.5}$ to atmospheric conditions due to the In–O dual incorporation effect. Li-ion conductivity variations of both electrolytes before and after exposure tests were also analyzed via AC impedance. Stainless steel (ST) was selected as the blocking electrode to assemble ST/solid electrolyte/ST symmetric cells. After exposure, both electrolytes demonstrate increased total resistance compared to the bare materials. In addition, $Li_{5.54}In_{0.02}PS_{4.47}O_{0.03}Cl_{1.5}$ shows much smaller resistance than that of the exposed $Li_{5.5}PS_{4.5}Cl_{1.5}$. As illustrated in Figure 2d, bare $Li_{5.5}PS_{4.5}Cl_{1.5}$ electrolyte shows a significant drop of Li-ion conductivity from 9.0 mS cm^{-1} to 0.9 mS cm^{-1} after a 20-minute exposure, merely representing 10.0% retention of its original value. Conversely, Li-ion conductivity of $Li_{5.54}In_{0.02}PS_{4.47}O_{0.03}Cl_{1.5}$ decreases from 7.5 mS cm^{-1} to 4.2 mS cm^{-1} after the same process, which is a superior performance in terms of the final value (4.2 mS cm^{-1} vs. 0.9 mS cm^{-1}) and retention (56.0% vs. 10.0%) than that of pristine $Li_{5.5}PS_{4.5}Cl_{1.5}$. Our investigation reveals that the $Li_{5.54}In_{0.02}PS_{4.47}O_{0.03}Cl_{1.5}$ electrolyte retains its high ionic conductivity after air exposure, which can be attributed to the minimal generation of impurities. In contrast, the undoped $Li_{5.5}PS_{4.5}Cl_{1.5}$ electrolyte exhibits inferior stability. Upon air exposure, it yields a higher concentration of impurities, leading to a decrease in ionic conductivity. This phenomenon is corroborated by the results depicted in Figure 2c and 2d, where a reduction in ionic conductivity to half of its original value is observed in the following exposure. Although the ionic conductivity decrement is partly due to the emergence of impurity phases, but the conductivity is not being entirely dependent on structural changes. The phase transition in the modified $Li_{5.54}In_{0.02}PS_{4.47}O_{0.03}Cl_{1.5}$ samples is likely confined to the surface of the electrolyte, with a minor quantity that may not be detectable by XRD. $Li_{5.54}In_{0.02}PS_{4.47}O_{0.03}Cl_{1.5}$ exhibits excellent air stability compared to previously reported SSEs (summarized in Table S5). To evaluate in-

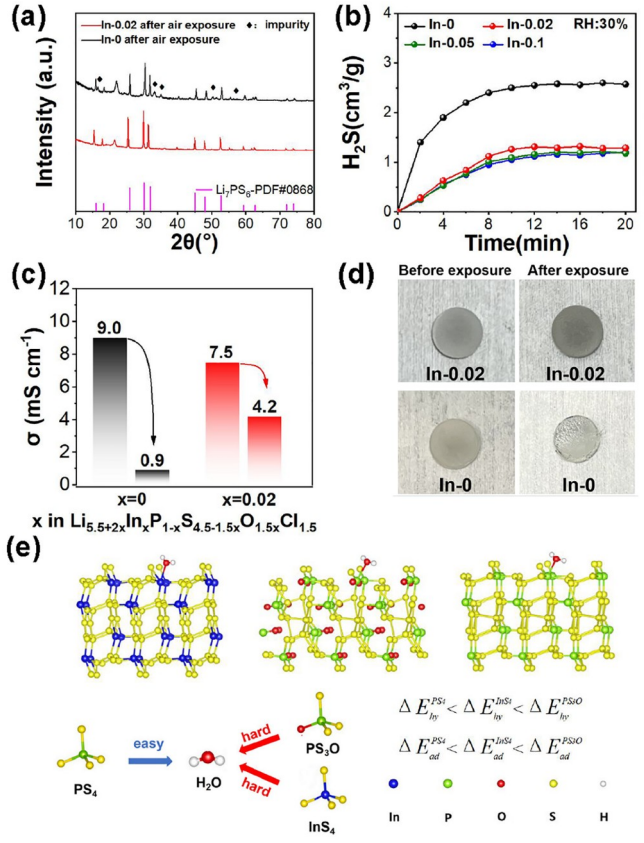

Figure 2 (Color online) (a) The amount of H_2S generated from the obtained materials with a testing humidity of 30% at room temperature and (b) digital photos of $Li_{5.5}PS_{4.5}Cl_{1.5}$ and $Li_{5.54}In_{0.02}PS_{4.47}O_{0.03}Cl_{1.5}$ solid electrolytes before and after the exposure in open air for 20 min. (c) XRD patterns of the prepared $Li_{5.5}PS_{4.5}Cl_{1.5}$ and $Li_{5.54}In_{0.02}PS_{4.47}O_{0.03}Cl_{1.5}$ solid electrolytes after the exposure in open air for 20 min or in dry room for 12 h. (d) Room-temperature Li-ion conductivity of the prepared $Li_{5.5}PS_{4.5}Cl_{1.5}$ and $Li_{5.54}In_{0.02}PS_{4.47}O_{0.03}Cl_{1.5}$ before and after air/dry room exposure. (e) Calculated models and corresponding adsorption and reaction energies of one water molecule on different units of $Li_{5.54}In_{0.02}PS_{4.47}O_{0.03}Cl_{1.5}$.

dustrial manufacturing property of the two electrolytes, their air/moisture stability in a dry room with a controlled dew point was further tested. Specifically, the exposure test was conducted in a dry room maintaining a dew point of −60 °C (RH: 0.2%) for 12 h. Although both materials suffer from similar trends of increased total resistance after the exposure, they exhibit much higher ionic conductivity retention rates at this lower dew point under a much longer storing durations (12 h vs. 20 min). The exposed $Li_{5.5}PS_{4.5}Cl_{1.5}$ maintains a Li-ion conductivity of 7.1 mS cm^{-1}, 78.9% of its original value, whereas $Li_{5.54}In_{0.02}PS_{4.47}O_{0.03}Cl_{1.5}$ shows a Li-ion conductivity of 6.9 mS cm^{-1} with an ionic conductivity retention as high as 92.0% (Figure 2d). Meantime, structural alteration of $Li_{5.5}PS_{4.5}Cl_{1.5}$ and $Li_{5.54}In_{0.02}PS_{4.47}O_{0.03}Cl_{1.5}$ following the above dry-room test was studied. Different from the results collected in open air (Figure 2c), the major diffraction peaks of $Li_{5.5}PS_{4.5}Cl_{1.5}$ stored in dry room agree well with the cubic argyrodite phase with small amounts of impurity. In contrast, such dry-room exposed $Li_{5.54}In_{0.02}PS_{4.47}O_{0.03}Cl_{1.5}$ shows a pure cubic argyrodite phase with negligible impurity. This underscores the efficacy of the In–O dual-doping approach in enhancing argyrodite's air/moisture stability, both in open-air and controlled dry-room conditions. Hence, optimizing the dew point of operating environment can greatly enhance the manufacturing properties of argyrodite-based SSBs [42]. Typically, the air/moisture stability for sulfide SSEs is linked with the electronegativity of O and S. Due to the higher electronegativity of O compared to S, combined with the stronger P–O bond than the P–S in the structure, the O-doped sample exhibits enhanced stability towards moisture. Moreover, calculating the water hydrolysis reaction energy (ΔE_{hy}) and adsorption energy (ΔE_{ad}) of different argyrodites is a good standard to investigate their air/moisture stability, it can reflect the variation of the sulfide after the H_2O attack by simplifying them to small units (PS_4, PS_3O, and InS_4). Therefore, density functional theory (DFT) method was utilized to compare the water hydrolysis reaction energy (ΔE_{hy}) and adsorption energy (ΔE_{ad}) of different argyrodites before and after In–O dual doping. Overall, sulfide SSEs that incorporate the PS_4 structural unit are susceptible to reactions with H_2O. Since three structural units (PS_4, PS_3O, and InS_4) are generated in LPSC-$In_{0.02}$, the energetics associated with the hydrolysis and adsorption reactions of the above SSEs in question adhere to the subsequent mathematical formulations:

$$E_{hy}^{PS_4} = E_{surface} + E_{H_2O} - E_{surface-PS_3O} - E_{H_2S} \quad (1)$$

$$E_{ad}^{PS_4} = E_{PS_4+H_2O} - E_{surface} - E_{H_2O} \quad (2)$$

In the formula, $E_{surface}$ represents the energy for surface structure, corresponding $E_{surface-PS_3O}$ is the surface structure energy after PS_4 is replaced by an O atom, and $E_{PS_4+H_2O}$ stands for the surface structure energy after binding to a water molecule. The adsorption and reaction energies of these units were computed individually through above equations (Table S4). As expected, PS_4 has the lowest ΔE_{hy} and ΔE_{ad}, which implies that PS_4 can easily react with water. In comparison, both the ΔE_{hy} and ΔE_{ad} of PS_3O show the highest value, verifying the feasibility of O-doping for air/moisture stability promotion. Besides, on the basis of the typical hard soft acid–base theory (HSAB), the doped In can act as a soft acid, which bonds with the soft-basic S easily, improving the electrolyte's chemical stability [23,43].

To further enhance the interfacial compatibility between Li metal and LPSC-$In_{0.02}$ in SSBs, InF_3 was employed to modify the surface of Li metal. Specifically, varying amounts of InF_3 powder were introduced to mix with molten lithium and kept at 300 °C for 5 min, resulting in the rapid formation of a complex interphase layer comprising Li–In alloys and LiF phases on Li surface, with the final product denoted as InF_3@Li (Figure 3a). The Li composites treated with varying

proportions of InF_3 dopants, ranging from 0% to 20%, are denoted as 0%InF_3@Li, 5%InF_3@Li, 10%InF_3@Li and 20% InF_3@Li, respectively. As depicted in Figure 3b, the dominant diffraction peaks observed in these XRD patterns correspond well to Li–In alloy, LiF, and Li metal, suggesting the successful synthesis of the target modified Li metal anode. Moreover, X-ray photoelectron spectroscopy (XPS) measurements corroborate the presence of these interphases on the Li anode. In the In 3d spectrum (Figure 3c), two primary peaks at 450.8 and 443.4 eV, along with two satellite peaks at 452.0 and 444.2 eV, are observed, indicating the presence of In^{3+} and Li–In alloy on lithium metal surface [44]. Additionally, a pronounced peak corresponding to LiF at 684.2 eV is discernible in the F 1s spectrum (Figure 3d), indicating the formation of LiF phase [45]. The digital photo in Figure 3e shows the dim surface of InF_3@Li at 300 °C. Upon natural cooling, the generation for the solidified lithium mass is discernible, which was subsequently pressed into a metallic foil for the assembly of ASSLMBs. Scanning electron microscopy (SEM) images demonstrate the smooth surface of the prepared InF_3@Li foil, and corresponding energy-dispersive spectroscopy (EDS) results disclose the homogenous distribution of In and F elements across the sample surface (Figure 3f). Atomic force microscopy (AFM) images confirm that the prepared 10%InF_3@Li exhibits a smoother surface than that of bare Li metal (Figure 3g, h), which facilitates a uniform Li platting/stripping. Moreover, the digital photographs of the as-prepared InF_3-10%@Li anode are presented in Figure S11, and the as-prepared modified anode shows a metallic luster and exhibits superior flexibility. CCD values of symmetric cells involving 5% InF_3@Li, 10%InF_3@Li, and 20%InF_3@Li anodes using LPSC-$In_{0.02}$ as the electrolyte were studied. The cells based on 5%InF_3@Li, 10%InF_3@Li, and 20%InF_3@Li display a CCD value of 1.4, 2.4 and 1.9 mA cm^{-2}, respectively (Figure S3). Notably, the 10%InF_3@Li/LPSC-$In_{0.02}$/10%InF_3@Li cell shows a higher CCD value than Li/LPSC-$In_{0.02}$/Li (2.4 mA cm^{-2} vs. 1.8 mA cm^{-2}), suggesting the enhanced stability of 10%InF_3@Li toward LPSC-$In_{0.02}$. Therefore, the optimized component 10%InF_3@Li is used for the following electrochemical tests. To make a concise discussion, 10% InF_3@Li is abbreviated as InF_3@Li. Additionally, long-term Li stripping/platting performance of Li/LPSC/Li, Li/LPSC-$In_{0.02}$/Li, and 10%InF_3@Li/LPSC-$In_{0.02}$/10%InF_3@Li sym-

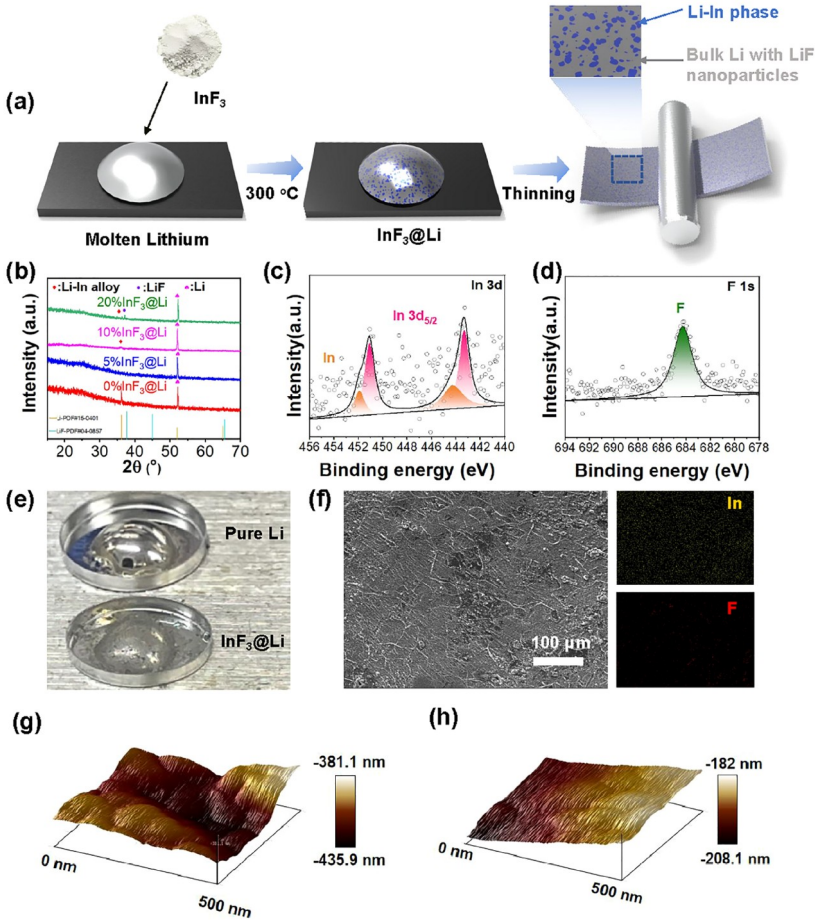

Figure 3 (Color online) Schematic illustrations of the whole fabrication procedure of the InF_3@Li composite. XRD patterns of the prepared (b) x%InF_3@Li (x = 0, 5, 10, 20). High-resolution XPS spectra of (c) In 3d and (d) F 1s of 10%InF_3@Li composite. (d) Digital photos of the as-prepared pure Li and 10% InF_3@Li. (f) SEM image of the obtained 10%InF_3 and corresponding EDS mapping of 10%InF_3@Li. AFM images of (g) pure Li and (h) 10%InF_3@Li.

metric cells was investigated under a current density of 0.1 mA cm^{-2} at a fixed area capacity of 0.1 mAh cm^{-2}. As exhibited at Figure S4a, the Li/LPSC/Li cell confronts a short cycling life for 10 h. After that, the cell experiences a sudden reduction of overpotentials, corresponding to the rapid infiltration of Li dendrites [46]. Conversely, both the Li/LPSC-$In_{0.02}$/Li and 10%InF_3@Li/LPSC-$In_{0.02}$/10%InF_3@Li cells demonstrate ultralong and stable Li stripping/platting performance over 1,000 h, albeit with obviously increased overpotentials. However, the latter cell exhibits slightly lower overpotential values at different selected durations (Figure S4b–S4d). These findings indicate that the In–O co-doped LPSC-$In_{0.02}$ electrolyte demonstrates superior compatibility with bare Li metal anode compared to LPSC electrolyte, and successfully, the optimized Li anode 10% InF_3@Li further increases the interfacial stability of the designed solid electrolytes.

The electrochemical performance of ASSLMBs utilizing $Li_{5.5}PS_{4.5}Cl_{1.5}$ (denoted as LPSC) and $Li_{5.54}In_{0.02}P_{0.98}S_{4.47}O_{0.03}Cl_{1.5}$ (denoted as LPSC-$In_{0.02}$) electrolytes in conjunction with bare Li metal and 10%InF_3@Li (denoted as InF_3@Li) anodes was validated. Corresponding NCM712/$Li_{5.5}PS_{4.5}Cl_{1.5}$/Li, NCM712/$Li_{5.54}In_{0.02}P_{0.98}S_{4.47}O_{0.03}Cl_{1.5}$/Li (denoted as 712/LPSC-$In_{0.02}$/Li), and NCM712/$Li_{5.54}In_{0.02}P_{0.98}S_{4.47}O_{0.03}Cl_{1.5}$/10%$InF_3$@Li (denoted as 712/LPSC-$In_{0.02}$/InF_3@Li) cells were assembled and cycled at various C-rates within the voltage range of 3.0–4.2 V (vs. Li^+/Li) at room temperature. These cells were first charged and discharged at 0.2 C. The cathode loading for every ASSLMBs is 2 mg (with active material being 1.4 mg). As illustrated at Figure 4a, the electrochemical polarizations of the three batteries, referring to the disparities between the charge and discharge plateaus at first cycle, exhibit a decreasing trend. 712/LPSC/Li exhibits the largest polarization, whereas 712/LPSC-$In_{0.02}$/InF_3@Li shows the lowest one. This discrepancy primarily arises from the stability of the interface on the anode side. LPSC-$In_{0.02}$ facilitates a faster Li-ion transport across the interface towards bare Li metal compared to LPSC due to the enhanced compatibility. Additionally, 10%InF_3@Li provides a more stable and rapid Li-ion diffusion dynamics with the complex interphase comprising Li-In alloy and LiF, resulting in further diminished polarization compared to bare Li metal. 712/LPSC/Li delivers an ultralow initial discharge capacity of 16.7 mAh g^{-1} (0.030 mAh cm^{-2}) with a Coulombic efficiency of 36.5%, and sustains 66.5% of its original capacity after 100 cycles. Conversely, 712/LPSC-$In_{0.02}$/Li shows a higher discharge capacity of 131.2 mAh g^{-1} (0.234 mAh cm^{-2}) and a Coulombic efficiency of 83.3% for the 1st cycle but suffers from a rapid capacity degradation in the following 100 cycles. In sharp contrast, 712/LPSC-$In_{0.02}$/InF_3@Li delivers the highest initial discharge capacity of 177.5 mAh g^{-1} (0.316 mAh cm^{-2}) and Coulombic efficiency of 88.0%. Moreover, after 100 cycles, it remains a discharge capacity as high as 146.9 mAh g^{-1} with a capacity retention of 82.8% (Figure 4b). Therefore, the incorporation of LPSC-$In_{0.02}$ electrolyte and 10%InF_3@Li anode endows the ASSLMB with significantly enhanced charge/discharge capacities (177.5 mAh g^{-1} vs. 131.2 mAh g^{-1} vs. 16.7 mAh g^{-1}), Coulombic efficiency (88.0% vs. 83.3% vs. 36.5%), and superior cycling performance among these three cell configurations. Furthermore, EIS was employed to elucidate the resistance variations for different parts in these three SSBs before and after 100 cycles. All these cells with the same cathode electrode exhibit similarly increased total resistances after 100 cycles. Therefore, the dominant reason for resistance variations before and after cycling is associated with the anode side. The interface of LPSC-$In_{0.02}$/InF_3@Li delivers the smallest resistance increase, while the resistance of $Li_{5.5}PS_{4.5}Cl_{1.5}$/Li interface shows the largest increase among the three cells. This result is consistent with the previous battery performance differences. Afterwards, the synergistic impact of In-modification in the rate performance of the fabricated ASSLMBs was also investigated. The batteries were cycled with step-by-step increased charge/discharge C-rates ranging from 0.1 C to 1.0 C. Figure 4c, d depict that 712/LPSC-$In_{0.02}$/Li exhibits higher discharge capacities and smaller polarizations than those of 712/LPSC/Li at the selected C-rates. This can be attributed to the improved lithium compatibility for the LPSC electrolyte by In–O dual doping. Moreover, after replacing the bare Li metal anode with 10%InF_3@Li, the corresponding cell displays higher charge/discharge capacities, lower polarizations, and superior cycling performance (Figure 4c–e). This indicates that InF_3 modification on Li anode greatly enhances the rate capability of LPSC-$In_{0.02}$-based ASSLMBs. Specifically, 712/LPSC-$In_{0.02}$/InF_3@Li delivers 187.1, 174.3, 160.1 and 145.1 mAh g^{-1} at 0.1 C, 0.2 C, 0.5 C and 1.0 C (corresponding to 0.334, 0.311, 0.285 and 0.259 mAh cm^{-2}), respectively. In comparison, 712/LPSC-$In_{0.02}$/Li exhibits discharge capacities of 141.0, 120.1, 87.6 and 54.1 mAh g^{-1} (corresponding to 0.251, 0.214, 0.156 and 0.096 mAh cm^{-2}), while 712/LPSC/Li only delivers discharge capacities of 104.2, 60.7, 9.0 and 0.1 mAh g^{-1} (corresponding to 0.185, 0.108, 0.016 and 0.001 mAh cm^{-2}), at the same C-rates, respectively. Obviously, 712/LPSC-$In_{0.02}$/InF_3@Li shows the highest capacity output among the three cells (Figure 4e). Long-term cycling tests at a high current density of 0.5 C were also investigated. Similarly, 712/LPSC/Li demonstrates low discharge capacities during the whole testing process with huge polarizations (Figure 4f, g) (because the activation process at the 1st and 2nd cycle, the 3rd was chosen as the charge/discharge curve). In contrast, 712/LPSC-$In_{0.02}$/Li delivers a greatly enhanced discharge capacity of 130.3 mAh g^{-1} (0.232 mAh cm^{-2}) and maintains 73.6% of its initial capacity at 0.5 C after 400 cycles. More importantly, 712/LPSC-$In_{0.02}$/InF_3@Li shows

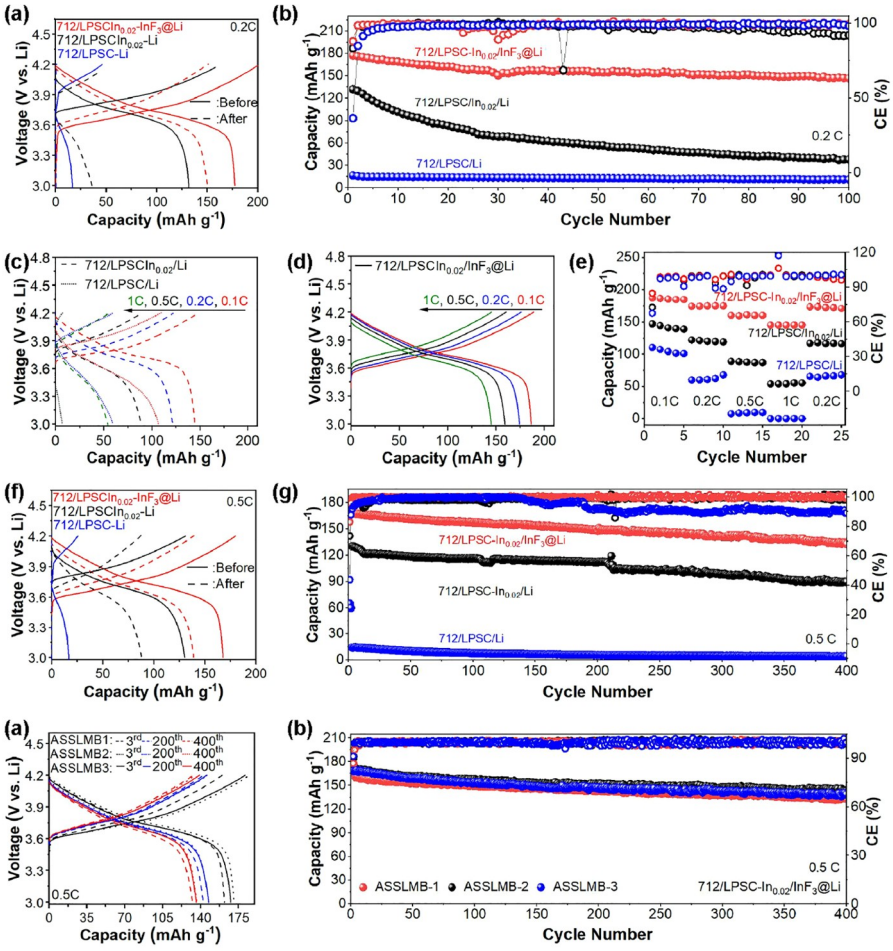

Figure 4 (Color online) (a) Charge/discharge profiles of the assembled 712/LPSC/Li, 712/LPSCIn$_{0.02}$/Li, and 712/LPSCIn$_{0.02}$/InF$_3$@Li cycled at 0.2 C between 3.0 and 4.2 V (vs. Li$^+$/Li) in the first cycle. (b) Long-term cycling performance of these cells. (c, d) Charge/discharge plots and (e) rate performance of 712/LPSC/Li, 712/LPSCIn$_{0.02}$/Li, and 712/LPSCIn$_{0.02}$/InF$_3$@Li cells at different C-rates between 3.0 and 4.2 V (vs. Li$^+$/Li). (f) Charge/discharge profiles of the third cycle of the assembled 712/LPSC/Li, 712/LPSCIn$_{0.02}$/Li, and 712/LPSCIn$_{0.02}$/InF$_3$@Li cells cycled at 0.5 C between 3.0 and 4.2 V (vs. Li$^+$/Li). (g) Corresponding cycling performance.

the highest discharge capacity (167.8 mAh g^{-1}/0.299 mAh cm^{-2}) and Coulombic efficiency (83.0%) in the first cycle. After 400 cycles, it retains a discharge capacity of 134.2 mAh g^{-1} (0.239 mAh cm^{-2}) with a capacity retention of 80.0%. This means that the cell employing In-modification strategy both on the solid electrolyte and Li anode contributes prominent promotion to discharge capacities and cycling performance with small interfacial resistance changes (Figure 4f, g and Figure S5d–S5f and S5h). Furthermore, electrochemical impedance spectroscopy (EIS) was conducted on both the pristine and cycled batteries to elucidate the alterations in resistance in various sections of the battery. As for the 712/LPSC-In$_{0.02}$/InF$_3$@Li cells, the EIS spectrum can be divided into the high frequency (MHz range), middle frequency, and low frequency regions (10−1 Hz). Four components are required for a sufficient fit of the spectrum, corresponding to an equivalent circuit of (R_{Bulk})(R_{Gb})-($R_{Cathode}$)(R_{Anode}) as shown in Figure S5. The modeled (R_{Bulk})-(R_{Gb})($R_{Cathode}$)(R_{Anode}) elements were assigned in accordance with previously suggested models by Tatsumisago *et al*. [47]. The high-frequency semicircle unequivocally corresponds to the bulk resistance of the solid electrolyte (R_{Bulk}). The resistance of the solid electrolyte (R_{Bulk}) is about 25 Ω for each sample, corresponding well to the high conductivity of the solid electrolyte. Moreover, a very small resistance, which is attributed to the grain boundary resistance of the cold-pressed sulfide solid electrolyte, is observed around high frequency. The semicircle in the low frequency region ($R_{Cathode}$/R_{Anode}) is assigned to the interface between the anode electrode and the solid electrolyte. The detailed impedance values of each part of 712/LPSC-In$_{0.02}$/anode before and after cycling are presented as a function of the testing periods in Table S7–S9. To verify the reliability of this In-modification strategy on ASSLMBs, three other pieces of cells with the same configuration were assembled and measured under the same conditions. As illustrated in Figure S8a, b, these cells exhibit similar exceptional electrochemical performance with highly repeatable charge/discharge capacities and cy-

cling performance. The assembled 712/LPSC-$In_{0.02}$/InF_3@Li ASSLMB in this work shows higher discharge capacity and much longer cyclability at a larger C-rate than those in the published papers (Table S6). Based on the above results, it appears that hindering Li dendrite growth and side reactions between argyrodite electrolytes and Li anode can effectively improve capacity properties, rate capability, and long-term cycling performance of ASSLMBs at different charge/discharge C-rates. Thereafter, the electrochemical performance of both $Li_{5.5}PS_{4.5}Cl_{1.5}$ (LPSC) and $Li_{5.54}In_{0.02}PS_{4.47}O_{0.03}Cl_{1.5}$ (LPSC-$In_{0.02}$) electrolytes after 12-h exposure to dry room towards InF_3@Li anode was evaluated. Specifically, ASSLMBs based on the exposed electrolytes were coupled with $LiNi_{0.7}Mn_{0.2}Co_{0.1}O_2$ (712) cathode and InF_3@Li anode and cycled between 3.0 and 4.2 V (vs. Li^+/Li) at room temperature. As illustrated in Figure S2a, b, the 712/LPSC(exposed)/InF_3@Li cell delivers a discharge capacity of 120.0 mAh g^{-1} with a Coulombic efficiency of 72.5% in the first cycle, maintaining 60.8% of its initial capacity after 400 cycles. In contrast, the 712/LPSC-$In_{0.02}$(exposed)/InF_3@Li cell exhibits promoted electrochemical performance with a higher initial discharge capacity of 158.8 mAh g^{-1} at 0.5 C and a Coulombic efficiency of 90.0%. Its discharge capacity sustains at 126.1 mAh g^{-1} with capacity retention of 79.4% after 400 cycles. These results indicate that the In–O dual-doping method can improve the air/moisture endurance of LPSC, which offers significantly boosted electrochemical performance in ASSLMBs compared to the pristine electrolyte. Additionally, EIS was performed on both batteries before and after 400 cycles to reveal their resistance variations. As exhibited in Figure S2c–e, the cell employing the exposed LPSC electrolyte shows significant increase of resistance after cycling, while the battery employing LPSC-$In_{0.02}$ exhibits much smaller interfacial resistance variations [48]. The rapid decay of discharge capacity observed in LPSC(exposed)-based SSBs can be ascribed to the increased resistance at electrolyte–cathode and electrolyte–anode interfaces, which originates from the degradation of solid electrolytes after exposure tests. Conversely, benefiting from the enhanced air/moisture tolerance through In–O doping, LPSC-$In_{0.02}$ demonstrates superior structural stability and high Li^+ conductivity retention. Consequently, it fosters exceptional electrolyte-involved solid/solid interfaces and battery performance (Figure S2b). This further proves the effectiveness of indium dual-processing strategy on the lithium metal stability and air stability. Moreover, the 712/LPSC$In_{0.02}$/InF_3@Li cells were assembled to further investigate the main role of indium plays during the cycling process. In Figure S10, compared to the 712/LPSC$In_{0.02}$/InF_3@Li cells, the assembled 712/LPSC$In_{0.02}$/In-Li cell shows higher specific capacities at the same C-rates. Specifically, it delivers discharge capacities of 168.4 mAh g^{-1} at 0.5 C, which proves that the use of high-content Indium alloy can lead to better electrochemical properties, which may be related to the closer contact between the alloy and the electrolyte.

In order to emphasize the role of LiF in the construction of stable hybrid interfacial phases, the In-doped Li was fabricated via the same melting-process. Figure S10a illustrates a standard melting fabrication procedure for a Li@In composite anode. It is evident that the indium metal, through the melting process, has been thoroughly incorporated into the lithium bulk, forming a Li–In alloy (denoted as Li@In). The indium content in the composite anode was confirmed to match the concentration used in our previous InF_3-doping steps (6.7% by mass, corresponding to 10% InF_3 doping). However, as shown in Figure S10b, c, under identical testing conditions, the electrochemical performance of using Li@In is far inferior to that of using InF_3 (0.4 mA cm^{-2} for CCD value and 28.7 mAh g^{-1} for the specific capacity). These differences in CCD and cycling performance can be explained by the diffusion of Li atoms inside the anode metal and the Li^+ at the SEI interphase. Within the bulk of the In-modified anode, the high ionic conductive characteristic of Li–In alloy in the anode with high ionic diffusion coefficient can quickly transport lithium from the bulk to the solid-state interface to compensate for the lithium depletion during stripping, thus ensuring tight interface contact and inhibiting the generation of gaps. However, an excessive concentration of indium particles can result in heightened electronic conductivity at the interface, accelerating lithium dendrite growth and ultimately degrading the interface. Therefore, as reported in the previous work [49], a stable interface should may form if the reaction products are electronically nonconductive or if the electronic conductivity is low enough to limit the growth of the interphase to a very thin film ("stable SEI"), an appropriate ratio of the formed reaction products, which can not only ensure good electronic insulation properties, but also ensure the rapid migration of ions at the interface, should be ensured. LiF with low electron conductivity ensures the stable solid-electrolyte interphase (SEI), and this stable interphase can homogenize current and Li^+ flux at the interface. For the Li@In metal, although the formation of Li–Ag alloy can ensure the efficient Li atom transport from bulk phase, without the protection of LiF interface, the Li@In metal is prone to react with the $Li_{5.5}PS_{4.5}Cl_{1.5}$ electrolyte to produce byproducts with high electronic conductivity, such as In particles [32]. This is also proves that the LiF interface guarantees excellent electronic insulation, resulting in the elimination of lithium dendrite formation caused by the concentration polarization under high current densities.

On one hand, we acknowledge that while indium plays a crucial role in enhancing the electrochemical stability of argyrodite-based lithium metal batteries, its high cost and elevated potential (0.6 V higher than that of lithium metal)

present challenges for commercial viability. The Figure S10 underscores the effectiveness of indium in improving battery performance; however, it also highlights the necessity to reduce indium content. Therefore, indium doping represents a promising avenue to improve both the stability and economic feasibility of all-solid-state batteries (ASSBs). By integrating this approach with advanced anode surface treatments, we aim to achieve a synergistic effect that enhances electrochemical stability and lithium metal compatibility of the electrolyte, thus mitigating the need for high indium content. For looking toward commercialization, it is imperative to develop batteries that not only offer exceptional performance but also meet market demands for cost-effectiveness and sustainability. Therefore, our strategy endeavors to navigate the intricate balance between performance optimization and commercial pragmatism.

To further verify our assumption on the surface morphology variations of the anode and SSEs, SEM and EDS mapping were performed on the surface of fresh and cycled anodes. Before cycling, both bare Li metal and fresh InF_3@Li show a smooth and flat surface (Figure 5a–c), while many cracks and Li dendrites can be clearly observed on the surface of the cycled LPSC/Li and LPSC-$In_{0.02}$/Li. Corresponding EDS results indicate that the impurities are mainly composed of P, S, and Cl with inhomogeneous distributions. Although a large number of cracks and dendrites appear on the LPSC-$In_{0.02}$/Li surface, but its morphology was better preserved than that of LPSC/Li. It seems that LPSC-$In_{0.02}$ can mitigate the growth of Li dendrites but cannot totally suppress side reactions. In contrast, InF_3@Li exhibits uniform and dense deposit coverage on the surface initially, and no obvious change is observed after cycling (Figure 5c). Corresponding element mapping images further reveal that In, P, and S are uniformly distributed on the anode, suggesting the formation of LiF and Li–In alloys on the anode surface. Consequently, such InF_3-modified anode together with the In-doping electrolyte can effectively mitigate side reactions between Li metal anodes and electrolytes and suppress Li dendrite growth during cycling.

To better understand the compatibility of In-modification strategy at the anode side, XPS analysis was performed on both $Li_{5.5}PS_{4.5}Cl_{1.5}$ and $Li_{5.54}In_{0.02}PS_{4.47}O_{0.03}Cl_{1.5}$ before and after cycling. As shown in Figure 5d–g, before cycling, the peaks in P 2p and S 2p spectra are consistent with the

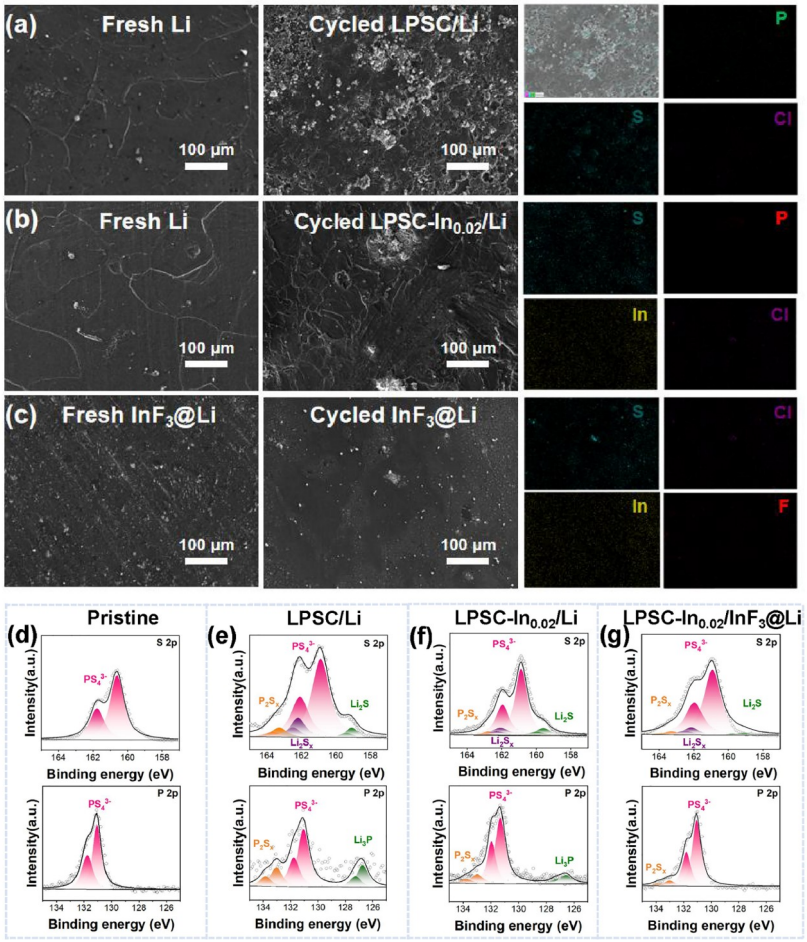

Figure 5 (Color online) Top-view SEM images of (a) LPSC/Li, (b) LPSC-$In_{0.02}$/Li and (c) LPSC-$In_{0.02}$/InF_3@Li interface before and after cycling. XPS evaluation on (d) pristine, (e) LPSC/Li, (f) LPSC-$In_{0.02}$Li and (g) LPSC-$In_{0.02}$/InF_3@Li interface after cycling.

characteristic peaks of PS_4^{3-} unit. P 2p and S 2p spectra for pristine LPSC, cycled LPSC/Li and LPSC-$In_{0.02}$/InF_3@Li are also shown in Figure 5e–g. Their primary peaks associating with the PS_4^{3-} unit in the S 2p spectra all remain. Besides, new peaks referring to Li_2S (159.4 eV), P_2S_x (163.4 eV) and Li_2S_x (162.5 eV) appear (Figure 5e, f, g). However, corresponding peak intensities of LPSC-$In_{0.02}$/InF_3@Li are lower than those of LPSC/Li and LPSC-$In_{0.02}$@Li, suggesting superior chemical/electrochemical stability on LPSC-$In_{0.02}$/InF_3@Li interface. Moreover, as shown in the P 2p spectrum of LPSC/Li and LPSC-$In_{0.02}$@Li, a certain amount of doublet peaks due to the phosphate and reduced phosphorus species near 131.4 eV are observed, suggesting the oxidation of LPSC during electrochemical cycling. Moreover, the semi-quantitative XPS analysis of the interphases for the pristine and cycled batteries at Figure S9 further demonstrates distinct levels of decomposition at the LPSC-$In_{0.02}$@Li and LPSC/Li interfaces after cycling. Notably, the cycled LPSC/InF_3@Li interface exhibits only minor alterations, indicating that the PS_4^{3-} content has been effectively preserved (Figure S9). The above XPS results reveal the formation of Li_2S and P_2S_x by side reactions between LPSC and bare Li metal, which agrees well with previous EDS mapping results, further validating that In-modification strategy on both SSE and Li anode enables better suppression of interfacial side reactions.

To unravel the working mechanism of the In-modification effect on the electrochemical performance of different ASSMLBs, the ionic transport kinetics and electrical distributions at the Li-metal-involved interface were carefully investigated. Firstly, DFT calculation was employed to study the Li migration behavior at LPSC-$In_{0.02}$/InF_3@Li interface. Specifically, the (002) lattice plane of LiCl, (110) lattice plane of Li–In, and (200) lattice plane of LiF were selected for the climbing image-nudged elastic band (CI-NEB) calculations due to their lowest surface energies [44]. Based on the calculations, the energy barriers were determined and compared. As illustrated in Figure 6b, c, LiF and LiCl exhibit relatively high diffusion energy barrier values of 0.79 eV and 0.53 eV for Li-ion migrations. Consequently, the complex interphase layer containing LiF and LiCl between the SSE and lithium metal anode negatively impacts the rapid transfer of lithium ions, consequently impeding the proliferation of Li dendrite growth at the interface. Typically, Li–In is chosen as a common anode material in sulfide-based ASSLMBs due to its superior compatibility with sulfide electrolytes [27]. Here, the low energy barrier of Li–In (0.14 eV) obtained from the simulation suggests a fast diffusion rate for Li across the interface containing Li–In. Thus, the *in-situ* generated Li–In facilitates a homogeneous deposition of Li^+ and fast Li transport during cycling in ASSLMBs. Though the In-doped LPSC SSEs reacts with lithium anodes to produce LiCl-containing interphases and inhibit Li dendrite growth, however, the enhanced inhibition of Li dendrites is not sufficiently robust to withstand high current densities (C-rates). The impact of this effect is reflected by the corresponding NCM712/LPSC-$In_{0.02}$/Li cell, which exhibits higher discharge capacities and superior cycling performance at low current densities (C-rates) compared to NCM712/LPSC/Li (Figure 4). However, this cell still experiences rapid capacity degradation at high C-rates. Additionally, it shows lower discharge capacities and even short-circuit at higher current densities. In contrast, 10%InF_3@Li generates considerable amounts of Li–In and a new Li-dendrite-inhibition species (LiF) at the interface towards LPSC-$In_{0.02}$, which was confirmed by the XPS results in Figure 5. The generation of LiF prevents the buildup of inactive Li, further reducing the Li dendrites growth. Moreover, the increased amount of Li–In alloy in the interphase facilitates fast Li transport dynamics across the interface [45]. The dual doping effect of In–O on the solid electrolyte and the Li surface modification with InF_3 result in a complex interphase layer consisting of LiCl, LiF and Li–In phases, which fosters uniform Li stripping/plating behavior and enhances Li mobility across the layer. Meantime, the finite element simulation is carried out using COMSOL Multiphysics to elucidate the role of this interface coating in controlling lithium deposition. From Figure 6d–f, noticeable hot spots (areas with elevated current density due to tip defects of commercial Li foil) are observed on the bare Li metal anodes [49]. Compared with the LPSC/Li interface in Figure 6d, the LPSC-$In_{0.02}$/Li interface shows a smaller local current density (Figure 6e), pertaining to more uniform Li deposition. This is associated with the reduction potential differences of Li and In. Since the reduction potential of Li (−3.04 V) is much lower than that of In (−0.34 V), Li preferentially reacts with In to form Li–In. In serves as the nucleation sites for Li deposition and guides Li growth, inhibiting the generation of Li dendrites at the SSE/Li interface. However, the quantity of In dopants in LPSC-$In_{0.02}$ is too small to generate Li–In alloy at the interface or within voids, which is likely to cause a continued growth of Li dendrites. Consequently, the concentration of Li ions, particularly in the vicinity of the untreated Li electrode surface, exhibits notable nonuniformity on LPSC-$In_{0.02}$/Li. In comparison, when combined with the InF_3@Li anode, the LPSC-$In_{0.02}$ electrolyte exhibits a uniform current distribution over the SSE/Li interface (Figure 6f). The elimination of tip defects in bare Li foil is achieved by reducing the local current density upon the anode. This ensures uniform electric potential distribution and mitigates the occurrence of localized high-voltage areas that could otherwise promote dendrite formation or non-uniform electrochemical reactions [49].

The In-modification strategy employed on both LPSC and Li metal facilitates enhanced compatibility between the SSE and the anode, which provides a smooth, homogeneous and fast migration of Li during cycling, lowering the risk of

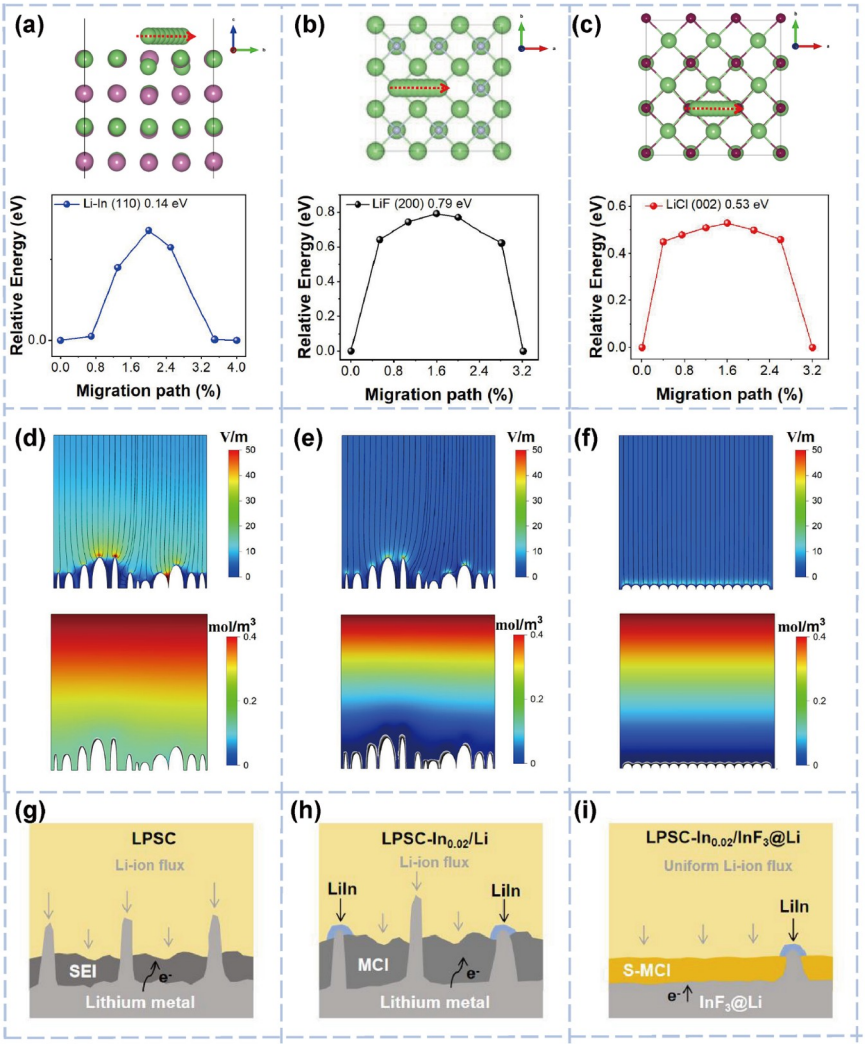

Figure 6 (Color online) Li migration barriers and the path of Li-ion migrating across different surfaces of (a) LiIn, (b) LiF and (c) LiCl. Finite element simulation analysis of the electrical field models and Li-ion concentration field models on (d) LPSC/Li, (e) LPSC-$In_{0.02}$/Li and (h) LPSC-$In_{0.02}$/InF_3@Li interface. Schematic illustration of the Li-ion flux and Li dendrite growth on the interfaces of (g) $Li_{5.5}PS_{4.5}Cl_{1.5}$/Li, (h) $Li_{5.54}In_{0.02}P_{0.98}S_{4.47}O_{0.03}Cl_{1.5}$/Li, and (i) $Li_{5.54}In_{0.02}P_{0.98}S_{4.47}O_{0.03}Cl_{1.5}$/10%$InF_3$@Li.

dendrite growth. In summary, possible work mechanism of the combined strategies is proposed based on the above experimental and simulation results (Figure 6g–i). Introducing In into LPSC can mitigate Li dendrite growth and facilitate Li-ion diffusion rate at a certain extent due to the generation of LiCl and Li–In phases in the interphase layer supported by sufficient partial electronic and ionic conductivity of the formed products, and the interphase may steadily grow "into" the solid electrolyte and thereby alter the properties of the whole bulk material. The formation of such a mixed conducting interphase (as we propose) is called MCI [50] (Figure 6g, h). However, this effect is not sufficient under a large Li-ion flux at large current density (C-rates). InF_3@Li metal can effectively enhance the Li dendrite inhibition capability and Li-ion diffusion rate across the SSE/Li interface due to the formation for complex LiCl–LiF–LiIn interphase with abundant LiF and Li–In species (denoted as stable reactive and mixed conducting interphase (S-MCI)) (Figure 6i).

Finally, electrochemical performance of the 712/LPSC-$In_{0.02}$/10%InF_3@Li cell at elevated (60 °C) and low temperature (−20 °C) was also investigated. At 60 °C, the cell shows a much higher initial discharge capacity than that works at room temperature (190.5 mAh g^{-1} vs. 167.8 mAh g^{-1}) at 0.5 C (Figure 7a). After 100 cycles, the cell maintains 79.4% of its original value at 0.5 C with a discharge capacity of 151.3 mAh g^{-1}. EIS results measured before and after cycling confirm that the resistance of the LPSC-$In_{0.02}$ solid electrolyte layer varies slightly and the major contribution of the total resistance increase comes from the interfacial resistance of the cathode mixture (Figure 7c). The cell also exhibits excellent electrochemical performance at low temperature. At the working temperature as low as −20 °C, the cell shows typical charge and discharge curves at different

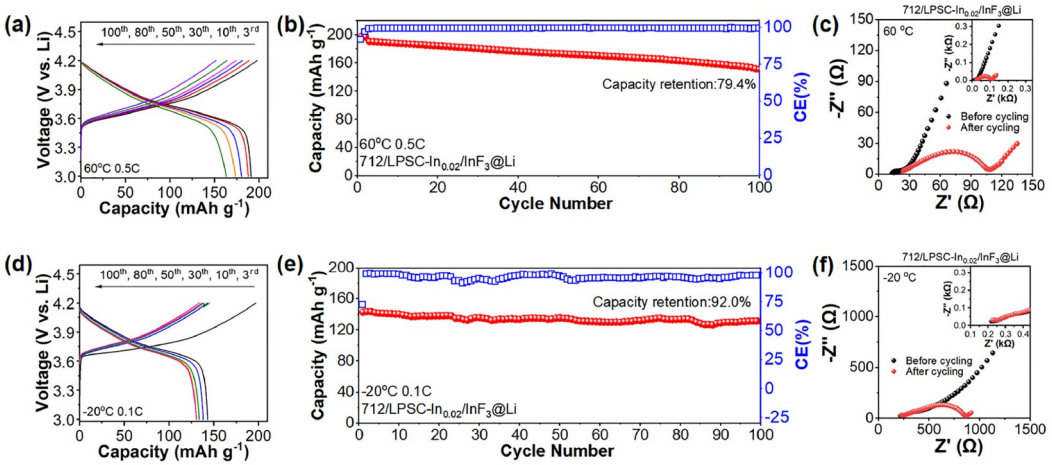

Figure 7 (Color online) Charge/discharge curves of the chosen cycles (the 3rd, 10th, 30th, 50th, 80th, and 100th cycle) of the assembled NCM712/$Li_{5.54}In_{0.02}P_{0.98}S_{4.47}O_{0.03}Cl_{1.5}$/10%$InF_3$@Li cell when cycled under (a) 60 °C at 0.5 C and (d) −20 °C at 0.1 C between 3.0 and 4.2 V (vs. Li^+/Li). Corresponding long-term cycling performance at (b) 60 °C and (e) −20 °C. EIS spectra of NCM712/$Li_{5.54}In_{0.02}P_{0.98}S_{4.47}O_{0.03}Cl_{1.5}$/10%$InF_3$@Li before and after 100 cycles under (c) 60 °C and (f) −20 °C.

cycles, with comparable electrode polarizations based on the voltage plateau differences (Figure 7d). It delivers an initial discharge capacity of 143.0 mAh g^{-1} at 0.1 C and maintains capacity retention of 92.0% after 100 cycles. Although the cell displays relatively lower discharge capacity at −20 °C than that of the cycled cell at elevated temperatures (room temperature (RT) and 60 °C), it exhibits superior cycling performance. The low discharge capacity is related to the decreased Li-ion conductivity of the LPSC-$In_{0.02}$ electrolyte, which may affect the ion diffusion behavior of the solid electrolyte-related interface both in the cathode mixture and the whole cell. The lowered Li-ion transport rate across solid/solid interfaces can destroy the Li intercalation/de-intercalation process, leading to a lower discharge capacity [50]. As a response to the decreased operating temperature, the increase of intrinsic resistance from LPSC-$In_{0.02}$ is minor. However, the electrolyte-related interfaces suffer from significant increase of resistance due to the decrease of LPSC-$In_{0.02}$ electrolyte and the increased resistance of the interfaces in electrode sections after cycling (Figure 7f). Moreover, based on our previous experience [5,6], batteries are more prone to the polarization at low temperatures [51–64]. To mitigate it, in the full-cell configurations, we strategically employed varying current densities: 0.5 C for both normal and elevated temperatures, and 0.1 C for low temperatures. This approach, informed by the reduced side reactions and lesser volume changes at lower temperatures, enhances the overall stability of the battery compared to that observed at higher temperatures [65], which contributes to the cell's excellent cycling performance with a high capacity retention rate (92.0%) at −20 °C. Thereafter, *in-situ* EIS was employed on the 712/LPSC-$In_{0.02}$/InF_3@Li cell during the initial cycle at various operating temperatures. As illustrated in Figure S6, at elevated temperatures (RT and 60 °C), the battery shows lower total resistance at different chosen charge/discharge states. When the temperature drops to −20 °C, the cell exhibits higher total resistance, resulting in the smallest initial charge/discharge capacities caused by the sluggish Li-ion migration dynamics. Corresponding distribution of relaxation time (DRT) analysis was applied to identify the resistance contribution of different sections in a cell. Generally, peaks within the relaxation time constant range of 10^{-7}–10^{-5} s are associated with the conduction processes that contribute to bulk resistance of SSE layer and grain boundary resistance within SSE particles [50]. The consistent alignment of these sections across all temperatures demonstrates their high stability, aligning well with previous findings derived from the equivalent circuit model [45]. The peaks observed at 10^{-3}–1 Hz are assigned to ion transport across the cathode (10^{-3}–10^{-2} Hz) and the anode (10^{-2}–1 Hz) interfaces [45]. Furthermore, an additional peak exists between 1 and 10 s at all three sets of temperatures, which is mainly due to the evolution of the feedback diffusion impedance [45]. The intensity distribution plots based on the DRT results are exhibited at Figure S6c, f, i, l to visually reveal the impedance contribution in each frequency band during the charging process. As demonstrated in Figure S6i, l, notable disparities were detected in the battery's cycling performance when subjected to a temperature of 60 °C: only a solitary overlapping peak is discerned in the time constant between 10^{-7} s and 10^{-5} s, corresponding to the disappearance of grain boundary impedance. This validates the increase of ionic conductivity at high temperatures. In contrast, at low temperatures, the peak patterns behave in the most complicated form. The peaks around 10^{-3}–10^{-2} s are mainly related to the cathode interface, and its high peak intensity indicates that there is a significant overall decrease in ion migration kinetics at the cathode. Notably, the 712/

LPSC-$In_{0.02}$/InF_3@Li cell demonstrates a consistently low and unchanged peak profile between 10^{-2}–1 when cycled at various temperatures, validating the beneficial impact of the In-modification strategy on stabilizing Li anodes, even at low temperatures. This observation is in accordance with the previous results and further confirms the universality and the effectiveness of InF_3 modification over a large temperature range [66].

3 Conclusions

In summary, we have developed a modification strategy incorporating In compounds into both the LPSC electrolyte and Li metal anode to enhance their interfacial stability. First, In_2O_3 dual-doping is employed on LPSC to improve its compatibility with bare Li metal and enhance its air/moisture stability under different dew points. As a result, the co-doped LPSC-$In_{0.02}$ electrolyte deliver a CCD value of 1.8 mA cm^{-2} and ionic conductivity of 7.5 mS cm^{-1} with exceptional stability towards air/moisture. Upon the exposure to ambient air for 20 min, the LPSC electrolyte retains only 10.0% of its original conductivity, while the modified electrolyte demonstrates significantly higher conductivity retention of 56.0% under the identical test conditions. Even after the exposure to the open air for 12 h in a dry room with a dew point of −60 °C, it retains 92.0% of its initial value. Moreover, this exposed electrolyte enables high discharge capacity and excellent cycling performance in ASSLMBs. Simulation results validate that the improved air/moisture stability is a result of the substitution of P and S with In and O in the argyrodite structure, respectively. In and O effectively reduces the aggregation of Li ions, thereby mitigating Li dendrite growth by forming Li–In alloy and Li_2O at the interface or within voids. Consequently, the LPSC-$In_{0.02}$ electrolyte shows superior cycling performance compared to the LPSC electrolyte in lithium symmetric cells operated at various temperatures. Additionally, a surface treatment of Li metal with InF_3 was proposed to give the formation of abundant LiF species and Li–In alloys at the anode surface. The In–O dual-doped electrolyte and InF_3-modified Li metal anode synergistically establish complex interphases between the solid electrolyte and Li metal anode, resulting in exceptional electrochemical performance in both symmetric cells and ASSLMBs across different operating temperatures. Specifically, the 712/LPSC-$In_{0.02}$/InF_3@Li cell exhibits highly repeatable battery performance, delivering initial discharge capacities of 177.5 mAh g^{-1} and 167.8 mAh g^{-1} at 0.2 C and 0.5 C, and retains 82.8% and 80.0% of the original values after 100 and 400 cycles at room temperature, respectively. Moreover, this battery shows high initial discharge capacities of 190.5 mAh g^{-1} and 143.0 mAh g^{-1} when cycled at 0.5 C and 0.1 C under 60 °C and −20 °C, respectively, with capacity retention of 79.4% and 92.0% after 100 cycles. This study sheds light on the design of high-performance ASSLMBs capable of functioning across a wide temperature range.

Acknowledgements This work was supported by the National Key Research and Development Program (2021YFB2500200) and the National Natural Science Foundation of China (52177214, 52222703). We gratefully acknowledge the Analytical and Testing Center of HUST for us to use the facilities. The Basic Science Research Fund in Xidian University (ZYTS24132), the Postdoctoral Science Research Program of Shaanxi (30102230001).

Conflict of interest The authors declare no conflict of interest.

Supporting information The supporting information is available online at http://chem.scichina.com and http://link.springer.com/journal/11426. The supporting materials are published as submitted, without typesetting or editing. The responsibility for scientific accuracy and content remains entirely with the authors.

1 Goodenough JB, Kim Y. *Chem Mater*, 2009, 22: 587–603
2 Shen X, Zhang XQ, Ding F, Huang JQ, Xu R, Chen X, Yan C, Su FY, Chen CM, Liu X, Zhang Q. *Energy Mater Adv*, 2021, 2021: 2021/1205324
3 Bi CX, Hou LP, Li Z, Zhao M, Zhang XQ, Li BQ, Zhang Q, Huang JQ. *Energy Mater Adv*, 2023, 4: 0010
4 Chen S, Yu C, Wei C, Peng L, Cheng S, Xie J. *Chin Chem Lett*, 2023, 34: 107544
5 Liao C, Yu C, Miao X, Chen S, Peng L, Wei C, Wu Z, Cheng S, Xie J. *Materialia*, 2022, 26: 101603
6 Peng L, Ren H, Zhang J, Chen S, Yu C, Miao X, Zhang Z, He Z, Yu M, Zhang L, Cheng S, Xie J. *Energy Storage Mater*, 2021, 43: 53–61
7 Ohno S, Helm B, Fuchs T, Dewald G, Kraft MA, Culver SP, Senyshyn A, Zeier WG. *Chem Mater*, 2019, 31: 4936–4944
8 Peng L, Chen S, Yu C, Liao C, Sun M, Wang HL, Zhang L, Cheng S, Xie J. *J Power Sources*, 2022, 520: 230890
9 Wei C, Chen S, Yu C, Wang R, Luo Q, Chen S, Wu Z, Liu C, Cheng S, Xie J. *Appl Mater Today*, 2023, 31: 101770
10 Wei C, Wang R, Wu Z, Luo Q, Jiang Z, Ming L, Yang J, Wang L, Yu C. *Chin Chem Lett*, 2024, 35: 108717
11 Wei C, Yu C, Chen S, Chen S, Peng L, Wu Y, Li S, Cheng S, Xie J. *Electrochim Acta*, 2023, 438: 141545
12 Luo Q, Ming L, Zhang D, Wei C, Wu Z, Jiang Z, Liu C, Liu S, Cao K, Zhang L, Yu C, Cheng S. *Energy Mater Adv*, 2023, 4: 0065
13 Ming L, Liu D, Luo Q, Wei C, Liu C, Jiang Z, Wu Z, Li L, Zhang L, Cheng S, Yu C. *Chin Chem Lett*, 2023, 35: 109387
14 Luo Q, Liu C, Wei C, Wu Z, Wang Y, Li L, Jiang Z, Ming L, Yang J, Zhang L, Chen X, Cheng S, Yu C. *J Power Sources*, 2024, 608: 234616
15 Albertus P, Babinec S, Litzelman S, Newman A. *Nat Energy*, 2017, 3: 16–21
16 Lin D, Liu Y, Cui Y. *Nat Nanotech*, 2017, 12: 194–206
17 Liu J, Bao Z, Cui Y, Dufek EJ, Goodenough JB, Khalifah P, Li Q, Liaw BY, Liu P, Manthiram A, Meng YS, Subramanian VR, Toney MF, Viswanathan VV, Whittingham MS, Xiao J, Xu W, Yang J, Yang XQ, Zhang JG. *Nat Energy*, 2019, 4: 180–186
18 Lu P, Wu D, Chen L, Li H, Wu F. *Electrochem Energy Rev*, 2022, 5: 3
19 Ahmad N, Sun S, Yu P, Yang W. *Adv Funct Mater*, 2022, 32: 2201528
20 Peng L, Chen S, Yu C, Wei C, Liao C, Wu Z, Wang HL, Cheng S, Xie J. *ACS Appl Mater Interfaces*, 2022, 14: 4179–4185
21 Sun Z, Lai Y, Lv N, Hu Y, Li B, Jiang L, Wang J, Yin S, Li K, Liu F. *ACS Appl Mater Interfaces*, 2021, 13: 54924–54935
22 Liu H, Zhu Q, Wang C, Wang G, Liang Y, Li D, Gao L, Fan LZ. *Adv Funct Mater*, 2022, 32: 2203858

23 Wei C, Yu C, Wang R, Peng L, Chen S, Miao X, Cheng S, Xie J. *J Power Sources*, 2023, 559: 232659
24 Zeng D, Yao J, Zhang L, Xu R, Wang S, Yan X, Yu C, Wang L. *Nat Commun*, 2022, 13: 1909
25 Wenzel S, Randau S, Leichtweiß T, Weber DA, Sann J, Zeier WG, Janek J. *Chem Mater*, 2016, 28: 2400–2407
26 Wang H, Gao H, Chen X, Zhu J, Li W, Gong Z, Li Y, Wang M-, Yang Y. *Adv Energy Mater*, 2021, 11: 2102148
27 Lu Y, Zhao CZ, Hu JK, Sun S, Yuan H, Fu ZH, Chen X, Huang JQ, Ouyang M, Zhang Q. *Sci Adv*, 2022, 8: eadd0510
28 Zhang JW, Wang WH, Xie MX, Wu HR, Wang YP, Bao HT, Cao BQ, Shao GQ. *Electrochim Acta*, 2023, 461: 142691
29 Luo S, Wang Z, Li X, Liu X, Wang H, Ma W, Zhang L, Zhu L, Zhang X. *Nat Commun*, 2021, 12: 6968
30 Liu J, Zhao H, Xia J, Yi L, Chen X, Li D, Ni S, Su X, Chen Y, Liu M, Wang X. *J Energy Chem*, 2024, 94: 758–767
31 Guo Z, Wang T, Wang D, Xu H, Liu X, Dai Y, Yang H, Huang Y, Luo W. *ACS Nano*, 2023, 17: 14136–14143
32 Jin S, Ye Y, Niu Y, Xu Y, Jin H, Wang J, Sun Z, Cao A, Wu X, Luo Y, Ji H, Wan LJ. *J Am Chem Soc*, 2020, 142: 8818–8826
33 Han SY, Lee C, Lewis JA, Yeh D, Liu Y, Lee HW, McDowell MT. *Joule*, 2021, 5: 2450–2465
34 Hänsel C, Singh B, Kiwic D, Canepa P, Kundu D. *Chem Mater*, 2021, 33: 6029–6040
35 Li Z, Jiang X, Lu G, Deng T, Wang R, Wei J, Zheng W, Yang Z, Tang D, Zhao Q, Hu X, Xu C, Zhou X. *Chem Eng J*, 2023, 465: 142895
36 Chen T, Zhang L, Zhang Z, Li P, Wang H, Yu C, Yan X, Wang L, Xu B. *ACS Appl Mater Interfaces*, 2019, 11: 40808–40816
37 Khurram Tufail M, Ahmad N, Zhou L, Faheem M, Yang L, Chen R, Yang W. *Chem Eng J*, 2021, 425: 130535
38 Wei C, Wang R, Wu Z, Luo Q, Jiang Z, Ming L, Zhang L, Lu H, Li G, Li L, Yu C, Cheng S. *Chem Eng J*, 2023, 476: 146531
39 Smith JG, Siegel DJ. *Nat Commun*, 2020, 11: 1483
40 Wang S, Wu Y, Ma T, Chen L, Li H, Wu F. *ACS Nano*, 2022, 16: 16158–16176
41 Zhao F, Liang J, Yu C, Sun Q, Li X, Adair K, Wang C, Zhao Y, Zhang S, Li W, Deng S, Li R, Huang Y, Huang H, Zhang L, Zhao S, Lu S, Sun X. *Adv Energy Mater*, 2020, 10: 1903422
42 Randrema X, Mfiban IL, Soler M, Profatilova I, Berthault M, Ramos R, Lavie J, De Vito E, Blanc L, Diry S, Launois S, Tarnopolskiy V, Reytier M, Colin JF, Barchasz C, Liatard S. *Batteries Supercaps*, 2024, 7: e202300380
43 Liang J, Chen N, Li X, Li X, Adair KR, Li J, Wang C, Yu C, Banis MN, Zhang L, Zhao S, Lu S, Huang H, Li R, Huang Y, Sun X. *Chem Mater*, 2020, 32: 2664–2672
44 Wu Z, Liu C, Liu X, Jiang Z, Wei C, Luo Q, Li L, Yu L, Zhang L, Cheng S, Yu C. *J Power Sources*, 2024, 602: 234295
45 Wei C, Liu C, Xiao Y, Wu Z, Luo Q, Jiang Z, Wang Z, Zhang L, Cheng S, Yu C. *Adv Funct Mater*, 2024, 34: 2314306
46 Lu Y, Zhao CZ, Yuan H, Cheng XB, Huang JQ, Zhang Q. *Adv Funct Mater*, 2021, 31: 2009925
47 Sakuda A, Hayashi A, Tatsumisago M. *Chem Mater*, 2010, 22: 949–956
48 Ren Q, Tang X, He K, Zhang C, Wang W, Guo Y, Zhu Z, Xiao X, Wang S, Lu J, Yuan Y. *Adv Funct Mater*, 2023, 34: 2312220
49 Wenzel S, Leichtweiss T, Krüger D, Sann J, Janek J. *Solid State Ion*, 2015, 278: 98–105
50 Li S, Zhu H, Liu Y, Wu Q, Cheng S, Xie J. *Adv Mater*, 2023, 35: 2301967
51 Lu P, Gong S, Wang C, Yu Z, Huang Y, Ma T, Lian J, Jiang Z, Chen L, Li H, Wu F. *ACS Nano*, 2024, 18: 7334–7345
52 Jin Y, He Q, Liu G, Gu Z, Wu M, Sun T, Zhang Z, Huang L, Yao X. *Adv Mater*, 2023, 35: 2211047
53 Zhang Z, Wu L, Zhou D, Weng W, Yao X. *Nano Lett*, 2021, 21: 5233–5239
54 Zhao X, Shen L, Zhang N, Yang J, Liu G, Wu J, Yao X. *Energy Mater Adv*, 2024, 2024: 0074
55 Wei C, Xiao Y, Wu Z, Liu C, Luo Q, Jiang Z, Li L, Ming L, Yang J, Cheng S, Yu C. *Sci China Chem*, 2024, 67: 1990–2001
56 Koerver R, Aygün I, Leichtweiß T, Dietrich C, Zhang W, Binder JO, Hartmann P, Zeier WG, Janek J. *Chem Mater*, 2017, 29: 5574–5582
57 Gu Y, Hu J, Lai C, Li C. *Adv Energy Mater*, 2023, 13: 2203679
58 Liu Y, Meng J, Lei M, Yu Y, Lai C, Li C. *Adv Funct Mater*, 2023, 33: 2208013
59 Zhang Y, Meng J, Chen K, Wu H, Hu J, Li C. *ACS Energy Lett*, 2020, 5: 1167–1176
60 Merry TL, Hedges CP, Masson SW, Laube B, Pöhlmann D, Wueest S, Walsh ME, Arnold M, Langhans W, Konrad D, Zarse K, Ristow M. *Nat Commun*, 2020, 11: 3706
61 Xu P, Shuang ZY, Zhao CZ, Li X, Fan LZ, Chen A, Chen H, Kuzmina E, Karaseva E, Kolosnitsyn V, Zeng X, Dong P, Zhang Y, Wang M, Zhang Q. *Sci China Chem*, 2024, 67: 67–86
62 Xin S, Zhang X, Wang L, Yu H, Chang X, Zhao YM, Meng Q, Xu P, Zhao CZ, Chen J, Lu H, Kong X, Wang J, Chen K, Huang G, Zhang X, Su Y, Xiao Y, Chou SL, Zhang S, Guo Z, Du A, Cui G, Yang G, Zhao Q, Dong L, Zhou D, Kang F, Hong H, Zhi C, Yuan Z, Li X, Mo Y, Zhu Y, Yu D, Lei X, Zhao J, Wang J, Su D, Guo YG, Zhang Q, Chen J, Wan LJ. *Sci China Chem*, 2024, 67: 13–42
63 Chang X, Zhao YM, Yuan B, Fan M, Meng Q, Guo YG, Wan LJ. *Sci China Chem*, 2024, 67: 43–66
64 Xue T, Qian J, Guo X, Chen Y, Yu K, Yu T, Li Y, Li L, Wu F, Chen R. *Sci China Chem*, 2024, 66: 2121–2129
65 Wu Z, Chen S, Yu C, Wei C, Peng L, Wang HL, Cheng S, Xie J. *Chem Eng J*, 2022, 442: 136346
66 Wang R, Wu Z, Yu C, Wei C, Peng L, Wang L, Cheng S, Xie J. *Front Energy Res*, 2023, 10: 1108789